Mn_3O_4@$CoMn_2O_4$–Co_xO_y Nanoparticles: Partial Cation Exchange Synthesis and Electrocatalytic Properties toward the Oxygen Reduction and Evolution Reactions

Zhishan Luo[†], Erdem Irtem[†], Maria Ibáñez[†], Raquel Nafria[†], Sara Martí-Sánchez[⊥], Aziz Genç[⊥], Maria de la Mata[⊥],Yu Liu[†], Doris Cadavid[†], Jordi Llorca[∥], Jordi Arbiol[⊥▽], Teresa Andreu[†], Joan Ramon Morante[†#], and Andreu Cabot[*†▽]

[†] Catalonia Institute for Energy Research—IREC, Sant Adrià del Besòs, 08930 Barcelona, Spain

[∥] Institut de Tècniques Energètiques, Universitat Politècnica de Catalunya, 08028 Barcelona, Spain

[⊥] Catalan Institute of Nanoscience and Nanotechnology (ICN2), CSIC and The Barcelona Institute of Science and Technology (BIST), Campus UAB, Bellaterra, 08193 Barcelona, Spain

[#] Departament d'Electronica, Universitat de Barcelona, 08028 Barcelona, Spain

[▽] ICREA, Pg. Lluís Companys 23, 08010 Barcelona, Spain

Abstract

Mn3O4@CoMn2O4 nanoparticles (NPs) were produced at low temperature and ambient atmosphere using a one-pot two-step synthesis protocol involving the cation exchange of Mn by Co in preformed Mn3O4 NPs. Selecting the proper cobalt precursor, the nucleation of CoxOycrystallites at the Mn3O4@CoMn2O4 surface could be simultaneously promoted to form Mn3O4@CoMn2O4–CoxOy NPs. Such heterostructured NPs were investigated for oxygen reduction and evolution reactions (ORR, OER) in alkaline solution. Mn3O4@CoMn2O4–CoxOyNPs with [Co]/[Mn] = 1 showed low overpotentials of 0.31 V at −3 mA•cm–2 and a small Tafel slope of 52 mV•dec–1 for ORR, and overpotentials of 0.31 V at 10 mA•cm–2 and a Tafel slope of 81 mV•dec–1 for OER, thus outperforming commercial Pt-, IrO2-based and previously reported transition metal oxides. This cation-exchange-based synthesis protocol opens up a new approach to design novel heterostructured NPs as efficient nonprecious metal bifunctional oxygen catalysts.

1 Introduction

The development of highly active, low-overpotential, stable, and low-cost electrocatalysts based on abundant and conflict-free raw materials is a critical challenge in several energy conversion technologies. In particular, high-performance bifunctional electrocatalysts for oxygen reduction and evolution reactions (ORR and OER) are an essential component in rechargeable metal–air batteries and regenerative low-temperature fuel cells.(1-6) In these devices, the use of a catalyst based on scarce and high-cost platinum group metals represents a severe cost constraint that strongly limits deployment. Alternative cost-effective and abundant transition metal oxides have been recently shown as outstanding candidates for ORR and/or OER in alkaline media. Some transition metal oxides show excellent stability, very high activity, low overpotential, and large roundtrip efficiency associated with their multiple possible oxidation states, off-stoichiometric compositions, defects, and vacancies.(7-14)

Among transition metal oxides, Mn-based oxides and particularly spinels have shown outstanding performance for ORR and, to a minor extent, for OER.(7, 15-21) Besides, Co-based oxides are excellent electrocatalysts for OER,(22-25) although particular Co-based catalysts have also shown excellent properties as bifunctional OER/ORR catalysts.(26-29) For instance, Co_3O_4 NPs supported on graphene demonstrated excellent electrocatalyst not only for OER but also for ORR.(8) Outstanding performances were also demonstrated from Co_3O_4 nanoparticles (NPs) on carbon nanofibers and Vulcan carbon as oxygen catalysts in zinc–air batteries.(30)

The combination of Mn and Co oxides, among other applications,(31-34) may thus provide excellent ORR/OER activities useful for a range of technologies.(35-43) In this direction, Cheng et al. demonstrated that $Co_xMn_{3-x}O_4$ NPs have considerable catalytic activity toward ORR and OER.(9) Liang et al. demonstrated $MnCo_2O_4$–graphene hybrids to be excellent electrocatalysts for ORR.(35) D. Wang et al. produced Co_2MnO_4–Co_3O_4 nanocomposites and demonstrated their excellent performance as bifunctional oxygen electrocatalyst.(22) Y. Wang et al. showed MnO_x–Co_3O_4 supported on carbon to outperform MnO_x/C and Co_3O_4/C catalysts in the ORR.(36) Xiao et al. produced Mn_3O_4–CoO core–shell structures and demonstrated that they have high performance in the ORR.(37) $Mn_{1.5}Co_{1.5}O_4$ oxides were produced by Xu et al., who also evaluated their electrocatalytic ORR performance.(38) In another excellent work, Menezes et al. demonstrated that tetragonal $CoMn_2O_4$ catalyst outperforms $MnCo_2O_4$ in the ORR but $MnCo_2O_4$outperforms $CoMn_2O_4$ in the OER.(39) Zhao et al.

also produced spinel Mn–Co oxides and demonstrated their superior bifunctional electrocatalytic properties when supported on N-doped carbon nanotubes.(10) Recently, C. Li et al. demonstrated the phase and composition control of cobalt manganese spinel NPs to provide improved oxygen electrocatalysis performances.(14) G. Li et al. probed Co_3O_4–Mn_3O_4 composites having discovered their excellent performance as oxygen electrocatalysts in zinc–air batteries.(40) MnO_2–CoO supported on reduced graphene oxide was also demonstrated as an excellent catalyst for ORR,(41) and $CoMn_2O_4$ nanodots on graphene showed efficient ORR and OER.(42) Interestingly, ordered CoMnO NPs within a nitrogen carbon framework also showed excellent OER activity.(11) Ge et al. also showed $MnCo_2O_4$ supported on nanocarbon supports to be an excellent electrocatalyst for ORR and OER.(43)

However, the multiple valence and related structural variability of transition metal oxides, which is at the origin of their exceptional electrocatalytic performance, is also behind the difficulty to produce these compounds in a reproducible and controlled manner. This is a particularly important limitation when taking into account the strong dependence of the physicochemical properties of transition metal oxides on composition, structural parameters, and distribution and oxidation state of cations. Besides, beyond performance and reproducibility, to ensure technological relevance, materials with large surface areas to maximize activity need to be produced in a cost-effective manner, what requires the synthesis of NPs using low reaction temperatures and ambient pressures.

In this work, we detail a scalable, low-temperature, and ambient pressure protocol to produce monodisperse Mn_3O_4@$CoMn_2O_4$ and Mn_3O_4@$CoMn_2O_4$–Co_xO_y NPs with controlled composition and phase distribution. We characterized the ORR and OER performance in alkaline solution of such heterostructured NPs performance to demonstrate their superior activity and durability when compared with benchmark electrocatalysts.

2 Experimental Section

Chemicals

Manganese(II) acetate ($Mn(OAc)_2$, 98%), cobalt(II) perchlorate hexahydrate ($Co(ClO_4)_2 \cdot 6H_2O$), xylenes (≥98.5%), cobalt(II) chloride hexahydrate ($CoCl_2 \cdot 6H_2O$, 98%), oleylamine (OLA, >70%), oleic acid (OA, 90%), Nafion (5%), and carbon-

supported Pt nanoparticles (Pt/C, 10 wt % Pt) were purchased from Sigma-Aldrich. The reference IrOx:/Ti dimensionally stable anode (DSA) electrocatalyst was obtained from ElectroCell Systems. Toluene, chloroform, and ethanol were of analytical grade and obtained from various sources. Milli-Q water was supplied by the PURELAB flex from ELGA. All chemicals were used as received without further purification, except OLA, which was purified by distillation.

Synthesis of Mn_3O_4@$CoMn_2O_4$ Core–Shell NPs

Mn_3O_4@$CoMn_2O_4$ core–shell NPs were synthesized by means of a one-pot two-step procedure. First Mn_3O_4 NPs were prepared similarly to previously reported procedures.(44) Briefly, xylene (15 mL), OLA (0.82 mL), OA (0.16 mL), and $Mn(OAc)_2$ (1 mmol) were placed in a 50 mL three-neck flask. Under air conditions, the solution was heated to 90 °C at 5 °C/min, the temperature at which deionized water (1 mL) was injected. The reaction mixture was maintain at 90 °C for 100 min to form Mn_3O_4 NPs. At this point, 1.0 M $CoCl_2{\cdot}6H_2O$ aqueous solution (1 mL) was added and the reaction was continued for an additional 300 min. Finally, the solution was cooled to room temperature, and NPs were purified by multiple precipitation/re-dispersion steps using toluene as solvent and ethanol as nonsolvent.

Synthesis of Mn_3O_4@$CoMn_2O_4$–Co_xO_y NPs

Mn_3O_4@$CoMn_2O_4$–Co_xO_y NPs were prepared following the exact same procedure but using a different cobalt precursor: $Co(ClO_4)_2{\cdot}6H_2O$. By tuning the Co:Mn molar ratio, NPs with different sizes and different compositions were obtained. In order to tune the Co:Mn molar ratio, we modified the concentration of the $Co(ClO_4)_2{\cdot}6H_2O$ aqueous solution between 0.5 and 2 M. The obtained Mn_3O_4@$CoMn_2O_4$–CoO NPs were denoted MC0.5, MC1, and MC2 referring to the Co:Mn molar ratios of 0.5, 1, and 2, respectively.

Structural and Chemical Characterization

Sizes and shapes of the initial NPs were examined by transmission electron microscopy (TEM) using a ZEISS LIBRA 120, operating at 120 kV. High-resolution TEM (HRTEM) studies were conducted using a field emission gun FEI Tecnai F20 microscope at 200 kV with a point-to-point resolution of 0.19 nm. Scanning electron microscopy (SEM) analyses were done in a ZEISS Auriga microscope with an energy dispersive X-ray spectroscopy (EDS) detector operating at 20 kV that allowed studying the NP composition. For SEM characterization, the materials were dispersed in chloroform and drop cast on silicon substrates. Powder X-ray diffraction (XRD) patterns

were collected directly from the as-synthesized NPs dropped on Si(501) substrate on a Bruker AXS D8 Advance X-ray diffractometer with Ni-filtered (2 μm thickness) Cu Kα radiation (λ = 1.5406 Å) operating at 40 kV and 40 mA. A LynxEye linear position-sensitive detector was used in reflection geometry. Nitrogen adsorption–desorption events were performed on a BEL-Mini adsorption analyzer. Thermogravimetric analysis was carried out on a Netzsch STA 449 F3 Jupiter analyzer. Hydrogen temperature-programmed reduction (TPR) was performed using a Micromeritics AutoChem HP 2950 chemisorption analyzer. A 20 mg amount of sample was pretreated at 100 °C for 30 min under an He flow of 50 mL/min. After cooling to room temperature, the samples were reduced in a flow of 12 vol % H_2/Ar (50 mL/min), and temperature was linearly increased at a rate of 10 °C/min up to 600 °C. X-ray photoelectron spectroscopy (XPS) was done on a SPECS system equipped with an Al anode XR50 source operating at 150 mW and a Phoibos 150 MCD-9 detector. The pressure in the analysis chamber was always below 10^{-7} Pa. The area analyzed was about 2 mm × 2 mm. The pass energy of the hemispherical analyzer was set at 25 eV and the energy step was set at 0.1 eV. Data processing was performed with the CasaXPS program (Casa Software Ltd., Teignmouth, U.K.). Binding energy (BE) values were centered using the C 1s peak at 284.8 eV. The atomic fractions (%) were calculated using peak areas.

Catalyst Preparation

The as-synthesized Mn–Co oxide NPs were mixed with carbon powder (Vulcan XC-72) with a weight ratio of 30% through sonication of NPs and carbon in chloroform and ethanol mixture (1:1). The NP/C composite was washed several times with chloroform and acetone. As formed NP/C nanocomposites were treated under air atmosphere at 180 °C for 5 h to remove surface organic ligands.(7) The catalyst ink for electrochemical measurements was prepared by mixing 5 mg of NP/C, 0.5 mL of deionized water, 0.5 mL of isopropanol, and 17.5 μL of 5 wt % of Nafion solution. The electrode was prepared by drop casting 10 μL of the catalyst ink on glassy carbon electrode, to afford a catalyst mass loading of approximately 275 mg·cm^{-2}. For comparison, electrodes with commercial Pt/C and an IrO_x-based catalyst (DSA, Electrocell A/S) were also prepared following the same experimental procedure.

Electrochemical Measurements

Electrochemical measurements were performed with a computer-controlled workstation bipotentiostats (VMP3 multichannel, BioLogic Instruments). A three-electrode system and rotator assembly (Pine rotator, AFMSRCE Pine Intruments) were used for electrochemical measurements containing a Teflon surrounded glassy carbon working

electrode (5 mm in diameter), a silver–silver chloride reference electrode (Ag/AgCl with 3.5 M KCl encapsulated, 012167 RE-1B, ALS Co. Ltd.-BAS Inc.), and a platinum wire for the counter electrode. The Ag/AgCl electrode was calibrated in a standard three-electrode system with two Pt wires used as working and counter electrodes and the Ag/AgCl electrode as reference electrode, using a 0.1 M KOH electrolyte saturated with pure H_2.(45) From linear scanning voltammetry at a scan rate of 0.1 $mV \cdot s^{-1}$, the thermodynamic potential (versus Ag/AgCl) for the hydrogen electrode reaction (potential at which the current crossed zero) was measured as −0.9863 V (Suppporting Information Figure S8). Then, potential was transformed to the reversible hydrogen electrode (RHE) scale as follows: $E_{RHE} = E_{Ag/AgCl} + 0.9863$ V. Both ORR and OER polarization curves were obtained in O_2-saturated 0.1 M KOH electrolyte. ORR experiments were tested from 0.1 to −0.55 V versus Ag/AgCl (i.e., 1.09 to 0.44 V versus RHE) at a scan rate of 5 $mV \cdot s^{-1}$ with different rotating rates (400–2000 rpm). OER polarization curves were obtained at potentials from 0.1 V versus Ag/AgCl (i.e., 1.09 V versus RHE) until current density reached 15 $mA \cdot cm^{-2}$ at a scan rate of 5 $mV \cdot s^{-1}$. To evaluate the catalyst durability, chronoamperometry was collected at 0.79 V versus RHE without rotation (0 rpm) in O_2-saturated 0.1 M KOH solution. For all measurements, the current density was *iR*-corrected ($R \approx 45\ \Omega$) using the solution resistance measured by EIS (electrochemical impedance spectroscopy) at open circuit potential with 5 mV amplitude over the frequency range of 200 kHz to 100 mHz.

3 Results and Discussion

Mn–Co oxide (MC) NPs were prepared by a one-pot, two-step process. First Mn_3O_4 NPs with octahedral geometries were produced by decomposing $Mn(OAc)_2$ at 90 °C in the presence of OLA, OA, and water.(44) In a second step, within the same flask and at the same temperature, an aqueous cobalt chloride ($CoCl_2 \cdot 6H_2O$) solution was added and allowed to react for 300 min. Panels a and b of Figure 1 show representative transmission electron microscopy (TEM) micrographs of the initial Mn_3O_4 NPs and those produced after adding an equivalent molar amount of Co chloride ([Co]/[Mn] = 1; MC1-Cl). Upon Co addition, the initial octahedral-shaped Mn_3O_4 NPs were slightly rounded (Figure 1a,b) without undergoing significant growth even for [Co]/[Mn] ratios up to 5. Annular dark field scanning TEM (ADF-STEM) in combination with electron energy loss spectroscopy (EELS) showed a core–shell type Co and Mn distribution with core and shell compositions compatible with Mn_3O_4 and

$CoMn_2O_4$ stoichiometries (Figure 1c). We observed no modification of the shell thickness when increasing the [Co]/[Mn] ratios above one, what points toward a self-limited reaction. High-resolution TEM (HRTEM) analysis showed Bragg reflections from two body centered tetragonal Mn_3O_4 phases (space group = $I4_1/amd$) with close lattice parameters. Upon filtering, a crystallographic epitaxial core–shell distribution was identified (Figure 1d). H_2 temperature-programmed reduction (TPR) profiles of Mn_3O_4 and MC1-Cl NPs were performed after ligand removal at 180 °C. H_2 TPR profile of Mn_3O_4 NPS showed two peaks, at 173 and 380 °C, which are associated with the reduction of low-coordinated surface and bulk Mn ions, respectively. MC1-Cl NPs did not present the 173 °C peak related to surface Mn ions in Mn_3O_4. However, it displayed the main Mn_3O_4 reduction peak at 380 °C and an additional peak at 490 °C, which can be associated with the reduction of a $CoMn_2O_4$ phase (Figure 1e).(46, 47)

When cobalt perchlorate ($Co(ClO_4)_2 \cdot 6H_2O$) instead of chloride was used as cobalt precursor, NPs with rougher surfaces were produced (Figure 2a–c). Upon Co perchlorate addition, a clear increase of the NP size was observed, with a final diameter depending on the amount of Co precursor used (Figures S1–S3). HRTEM and EELS mapping (Figure 2d,e) displayed a clear core–shell type element distribution with a central core phase and composition consistent with Mn_3O_4 and a Co-rich shell. At the NP surface, several crystallites with a CoO phase were evidenced (Figure 2e). H_2 TPR analysis of the MC/C samples after thermal treatment at 180 °C showed the main Mn_3O_4 and the $CoMn_2O_4$-related components and an additional peak at the reduction temperatures of Co_xO_y (300 °C, Figure 2f).(48-51)

From the structural and chemical characterization, we conclude that when reacting Mn_3O_4 with a solution of cobalt chloride or perchlorate in the above-defined conditions, a partial cation exchange between Mn^{2+} and Co^{2+} takes place at the Mn_3O_4 surfaces, to form a $CoMn_2O_4$ shell.(52) Besides, when compared with the Co chloride, the lower coordination ability of the perchlorate translates in a relatively higher reactivity of the Co ions in solution.(53-55) The higher propensity of Co^{2+} ions to incorporate to the oxide structure in the presence of the weaker perchlorate ion coordination makes the Co^{2+} ion uptake by cation exchange not fast enough, which results in the simultaneous nucleation of a cobalt oxide phase at the surface of the growing Mn_3O_4@$CoMn_2O_4$ structure. The initially nucleated cobalt oxide phase was identified as CoO by HRTEM, but it oxidized to Co_3O_4 with time and/or under mild thermal treatment. On the other hand, the lower reactivity of Co^{2+} in the presence of the more strongly coordinating chlorine ions prevented the nucleation of a Co_xO_y phase and constrained the Co incorporation to a self-limited partial cation exchange

reaction. Figure 3 shows a scheme of the growth mechanisms to produce either Mn_3O_4@$CoMn_2O_4$ or Mn_3O_4@$CoMn_2O_4$–Co_xO_y NPs.

Figure 4 shows the XRD pattern of as-synthesized Mn_3O_4, MC1-Cl, and MC1 NPs. XRD patterns revealed NPs to have a body centered tetragonal phase. Due to the peak broadening associated with the small crystal domains and the very similar unit cell parameters of Mn_3O_4 and $CoMn_2O_4$, XRD patterns were consistent with Mn_3O_4 (JCPDS No. 00-018-0803), Co_3O_4 (JCPDS No. 00-018-1538), and Mn–Co mixed oxides having spinel structure. On the other hand, CoO peaks (JCPDS No. 01-070-2856) could not be observed for any of the samples.

To study their electrocatalytic properties toward ORR and OER, NPs were supported on carbon powder (Vulcan XC-72) with a weight ratio of 30% through sonication of NPs and carbon in chloroform and ethanol (Figure S5). NP/C nanocomposites were then thermally treated under air atmosphere at 180 °C for 5 h to remove organic ligands. After this mild thermal treatment, no appreciable structural change was observed from TEM and XRD analyses (Figure S6). On the other hand, XPS analysis showed the presence of a main Co^{2+} component and an additional Co^{3+} contribution both before and after thermal treatment (Figure S7), which evidenced a partial oxidation of the cobalt ions at the $CoMn_2O_4$ and Co_xO_y surface. This oxidation was accentuated during the thermal treatment, with an increase of $[Co^{3+}]/[Co^{2+}]$ from 0.43 to 0.59. This oxidation is consistent with the H_2 TPR profiles also performed after the thermal treatment, since both CoO and Co_3O_4 phases show a similar reduction peak at 300 °C.(48-51) The final NP/C composites had specific surface areas and average pore sizes of around 140 m^2/g and 20 nm, respectively (Table S1).

The ORR activity of NP/C was measured in O_2-saturated 0.1 M KOH aqueous solution using a rotating disk electrode (RDE, Figures S9 and S10). Figure 5a shows linear sweep voltammograms (LSVs) of the different MC/C, and reference Mn_3O_4/C, Co_3O_4/C, and commercial Pt/C electrocatalysts. Figure 5b displays two ORR figures of merit, the current density at half-wave potential and the required overpotentials to reach −3 $mA \cdot cm^{-2}$. Yet, an extended summary of the electrochemical data is presented in Tables S1–S4. When compared with Mn_3O_4/C and Co_3O_4/C, the current density at half-wave potential and the required overpotentials to reach −3 $mA \cdot cm^{-2}$ clearly improved with the presence of the $CoMn_2O_4$ shell (MC1-Cl). In addition, the overpotentials at −3 $mA \cdot cm^{-2}$ of MC/C catalysts, including the Co_xO_yphase, were lower than those of MC1-Cl. In particular, the MC1/C catalyst outperformed the rest, showing the highest half-wave current densities, −2.77 $mA \cdot cm^{-2}$, and the lowest overpotential,

0.4 V. Higher Co_xO_y concentrations (MC2/C) maintained the large current density in the diffusion limited region but with a slightly higher overpotential.

Electrochemical kinetics was evaluated from Tafel slopes obtained from the middle ORR current density range, where the limitation by O_2 diffusion in the active layer was negligible (Figure S11). MC1/C exhibited a Tafel value of 52 mV·dec^{-1}, much lower than MC1-Cl/C (95 mV·dec^{-1}), Mn_3O_4/C (100 mV·dec^{-1}), Co_3O_4/C (124 mV·dec^{-1}), and even benchmark Pt/C (76 mV·dec^{-1}). The higher sensitivity of the electric current response to the applied potential for the MC1/C sample indicates this sample to have much more favorable kinetics. The lower Tafel slopes also indicate the ORR in this material to be most probably limited by a different reaction rate than in Mn_3O_4 or Co_3O_4, showing Tafel slopes closer to the 120 mV predicted when the formation of O_2^- is the rate-determining step.(56) The values obtained for MC1/C coincide with some of the best ORR Tafel values found in the literature, also associated with Mn-based oxide electrocatalysts under alkaline conditions.(57)

The electron transfer number (n_t) was calculated by Koutecky–Levich (K-L) method from the RDE current–potential curves at various rotation speeds (Figure S12).(58) Figure 5c shows n_t as a function of electrode potential from the slope of the resulting best-fit line, i.e., 0.45–0.7 V. The presence of $CoMn_2O_4$ on the Mn_3O_4 surface had a minor influence on n_t, which increased just slightly from bare Mn_3O_4/C to MC1-Cl/C. However, the presence of Co_xO_y at the Mn_3O_4@$CoMn_2O_4$ surface facilitated a rapid electron transfer, clearly shifting the ORR mechanism toward the four-electron pathway as evidenced by the increase of n_t values up to 3.68, 3.98, and 3.86 for MC0.5/C, MC1/C, and MC2/C, respectively.

In terms of stability, a critical requirement for practical applications, MC1/C and MC2/C catalysts showed current retention above 95% of the initial current after 20 h (Figure 5d), well above that of Mn_3O_4/C, Co_3O_4/C, MC1-Cl/C, and Pt/C catalyst, losing nearly half of its current density within the first 20 h (Figure 4d). Further, MC/C samples showed outstanding current retention 76% of the initial current compared to benchmark Pt/C catalyst, which lost 70% after 60 h durability test (Figure S13). For MC1/C and MC2/C, n_t values close to 4 revealed a direct O_2 reduction path and an advanced decomposition activity against deteriorating peroxide species, which is beneficial for holding a stable catalytic activity. On the contrary, in reference catalysts, the four-electron O_2 reduction into OH^- competed with the two-electron pathway yielding HO_2^- species which can induce electrode corrosion.(59, 60) Besides, LSV before and after a 20 h test showed no significant change either in the onset voltage or in current density

of both ORR and OER for MC0.5/C, MC1/C, and MC2/C electrocatalyts (Figure S14). A slight OER current density improvement was actually observed after a 20 h test, which we associate with the slow penetration of electrolyte into the film nanopores to meet additional catalytic sites.

Catalytic activities for OER are shown in Figure 6, including LSV driven to higher values than water oxidation standard potential, 1.23 V versus RHE and the corresponding Tafel plots. Co_3O_4/C showed state-of-the-art values, with an excellent catalytic activity, clearly outperforming that of Mn_3O_4/C. Since the Pt/C catalyst was not stable in OER, exhibiting an oxidation peak in the LSV,(61) an IrO_2-based commercial anode (Ti/IrO_2:Ta_2O_5, DSA) was tested as OER benchmark catalyst. This material showed exceptionally low onset voltages (0.25 V) and high current densities. On the other hand, all MC/C catalysts showed excellent OER performances close to the Co_3O_4 and DSA references, with low overpotentials (e.g., 0.31 V for MC1/C) and sharp current density increases. MC1/C exhibited a Tafel value of 81 $mV \cdot dec^{-1}$, clearly below that predicted for a single-electron rate-determining step, but slightly larger than lowest slopes obtained in literature, several of them using Ni-, Fe-, or Co-based electrocatalysts.(62, 63)Nevertheless, MC1/C showed the lowest Tafel slope from the materials tested here, with a value well below that of Mn_3O_4 (151 $mV \cdot dec^{-1}$) and MC1-Cl (106 $mV \cdot dec^{-1}$), but also of Co_3O_4 (110 $mV \cdot dec^{-1}$) and even DSA (104 $mV \cdot dec^{-1}$). This demonstrates the higher sensitivity to overpotential of the electrocatalytic activity of this material.

Overall, MC/C and MC-Cl/C composites clearly outperformed Mn_3O_4/C and Co_3O_4/C. We associate this fact with the presence of Co ions on the surface, which provide enhanced electron transfer capacity and strong coupling, thus resulting in more favorable reaction kinetics for OER. The better performance of MC/C over MC-Cl catalyst showed the addition of cobalt as a Co_xO_yphase to be particularly favorable. In particular, MC1/C exhibited the faster reaction kinetics, with a Tafel value of 81 $mV \cdot dec^{-1}$, clearly below that of Mn_3O_4, but also of that of Co_3O_4 and even DSA.

A main figure of merit for practical electrochemical and photoelectrochemical applications is the difference between the potential at ORR current density of −3 $mA \cdot cm^{-2}$ and that at OER current density of 10 $mA \cdot cm^{-2}$ ($\Delta E_{ORR-OER}$, Table 1). The smaller this difference, the closer a material is to being an ideal reversible catalyst. This value was 1.53 for Mn_3O_4/C and 1.07 for Co_3O_4. Lower $\Delta E_{ORR-OER}$ values were obtained for all the MC samples, especially for MC1/C, 0.85 V, which is among the best values reported (Tables S2–S4).

Electrocatalytic performance is boosted by enhancing charge transfer and increasing the number of available catalytic sites, i.e., proper energy band alignment and affinity for O_2/OH^-absorption. In this direction, cation ion doping and nanocrystallite surface decorating have provided relatively low onset potentials for spinel structures through increasing availability of catalytically active sites and their adsorption capabilities.(9, 15) In particular, the electrocatalytic activity of Co–Mn–O spinels was correlated with the oxygen binding ability on the catalyst surface.(9) Obviously, in such a complex catalyst, composition should be carefully adjusted to optimize performance in the two reactions. As an example, J. Li et al. calculated the OH^-adsorption energy of Co–Mn oxide with 1:1 ratio to be larger than that of pristine CoO and MnO, yet the trend was the opposite for the corresponding adsorption energy of O_2 molecule, suggesting that an optimum ratio must be reached to bridge these two abilities (ORR + OER).(11) Consistently with previous works, we found Mn_3O_4@$CoMn_2O_4$ to outperform Mn_3O_4 and Co_3O_4 catalysts in the ORR, but to be outperformed by the Co_3O_4 catalyst in the OER. However, Mn_3O_4@$CoMn_2O_4$–Co_xO_y catalysts reached OER performances above those of Co_3O_4, while simultaneously further enhancing ORR. The higher performance of Mn_3O_4@$CoMn_2O_4$–Co_xO_ycatalysts compared with Mn_3O_4@$CoMn_2O_4$ demonstrates Co_xO_y to play a key role in the electrocatatlyic performance. Besides, the lower performances obtained for Mn_3O_4@$CoMn_2O_4$–Co_xO_y materials with too high cobalt concentrations (MC2) demonstrate the availability of $MnCo_2O_4$ surface sites to also play an important role in the overall performance. Such uniquely heterogeneous nanocomposite structure, making strong interface coupling between Co_xO_y and spinel, can not only provide intrinsic electronic structure but also a favorable electronic transport capability. We hypothesize these improvements to be related with (i) a higher surface site density on the much rougher NP surface after Co_xO_y nucleation; (ii) an enhanced charge transfer from the lower band gap Co_xO_y; and (iii) a modified adsorption affinity for O_2 and OH^-that requires extensive computational work to be elucidated.

4 Conclusion

In summary, Mn_3O_4@$CoMn_2O_4$–CoO NPs were synthesized at low temperature and air atmosphere by the cation exchange of Mn by Co in preformed Mn_3O_4 NPs and the simultaneous growth of CoO crystallites at the Mn_3O_4@$CoMn_2O_4$ surface. Such hetereostructured NPs showed electrocatalytic activities for both ORR and OER in

alkaline media outperforming those of Mn_3O_4, Co_3O_4, and benchmark electrocatalysts. In particular, the optimized MC1 composition showed exceptionally low overpotentials, high current densities with excellent overall oxygen electrode activity and an improved durability. The cation-exchange-based synthesis protocol reported here with and without nucleation of secondary phases should be used as an additional tool to further aid precise engineering of complex heterostructured oxide catalysts directed toward optimizing their performance.

Acknowledgment

This work was supported by the European Regional Development Funds and the Spanish MINECO projects BOOSTER (ENE2013-46624-C4-3-R), TNT-FUELS (MAT2014-59961), e-TNT (MAT2014-59961-C2-2-R) and PEC-CO2 (ENE2012-3651). Z.L. and Y.L. thank the China Scholarship Council for scholarship support. E.I. thanks AGAUR for his Ph.D. grant (FI-2013-B-00769). M.I. thanks AGAUR for the Beatriu de Pinós postdoctoral grant (2013 BP-A00344). S.M. acknowledges funding from "Programa Internacional de Becas 'la Caixa'-Severo Ochoa". J.L. is a Serra Húnter Fellow and is grateful to ICREA Academia program. We also acknowledge the funding from Generalitat de Catalunya 2014 SGR 1638

References

1. Kraytsberg, A.; Ein-Eli, Y.The Impact of Nano-Scaled Materials on Advanced Metal–air Battery Systems*Nano Energy* **2013**, 2, 468– 480, DOI: 10.1016/j.nanoen.2012.11.016

2. He, Q.; Cairns, E. J.Review—Recent Progress in Electrocatalysts for Oxygen Reduction Suitable for Alkaline Anion Exchange Membrane Fuel Cells *J. Electrochem. Soc.* **2015**, 162, F1504– F1539, DOI: 10.1149/2.0551514jes

3. Yang, Z.; Nie, H.; Chen, X.; Chen, X.; Huang, S.Recent Progress in Doped Carbon Nanomaterials as Effective Cathode Catalysts for Fuel Cell Oxygen Reduction Reaction *J. Power Sources* **2013**, 236, 238–249, DOI: 10.1016/j.jpowsour.2013.02.057

4. Cheng, F.; Chen, J.Metal-Air Batteries: From Oxygen Reduction Electrochemistry to Cathode Catalysts*Chem. Soc. Rev.* **2012**, 41, 2172– 2192, DOI: 10.1039/c1cs15228a

5. Neburchilov, V.; Wang, H.; Martin, J. J.; Qu, W.A Review on Air Cathodes for Zinc–air Fuel Cells *J. Power Sources* **2010**, 195, 1271– 1291, DOI: 10.1016/j.jpowsour.2009.08.100

6. Jaouen, F.; Proietti, E.; Lefèvre, M.; Chenitz, R.; Dodelet, J.-P.; Wu, G.; Chung, H. T.; Johnston, C. M.;Zelenay, P.Recent Advances in Non-Precious Metal Catalysis for Oxygen-Reduction Reaction in Polymer Electrolyte Fuelcells *Energy Environ. Sci.* **2011**, 4, 114– 130, DOI: 10.1039/C0EE00011F

7. Zhu, H.; Zhang, S.; Huang, Y.-X.; Wu, L.; Sun, S.Monodisperse $M_xFe_{3-x}O_4$ (M = Fe, Cu, Co, Mn) Nanoparticles and Their Electrocatalysis for Oxygen Reduction Reaction *Nano Lett.* **2013**, 13, 2947–2951, DOI: 10.1021/nl401325u

8.Liang, Y.; Li, Y.; Wang, H.; Zhou, J.; Wang, J.; Regier, T.; Dai, H.Co_3O_4 Nanocrystals on Graphene as a Synergistic Catalyst for Oxygen Reduction Reaction *Nat. Mater.* **2011**, 10, 780– 786, DOI: 10.1038/nmat3087

9. Cheng, F.; Shen, J.; Peng, B.; Pan, Y.; Tao, Z.; Chen, J.Rapid Room-Temperature Synthesis of Nanocrystalline Spinels as Oxygen Reduction and Evolution Electrocatalysts *Nat. Chem.* **2011**, 3, 79– 84,DOI: 10.1038/nchem.931

10. Zhao, A.; Masa, J.; Xia, W.; Maljusch, A.; Willinger, M.-G.; Clavel, G.; Xie, K.; Schlögl, R.; Schuhmann, W.;Muhler, M.Spinel Mn-Co Oxide in N-Doped Carbon Nanotubes as a Bifunctional Electrocatalyst Synthesized by Oxidative Cutting *J. Am. Chem. Soc.* **2014**, 136, 7551– 7554, DOI: 10.1021/ja502532y

11. Li, J.; Wang, Y.; Zhou, T.; Zhang, H.; Sun, X.; Tang, J.; Zhang, L.; Al-Enizi, A. M.; Yang, Z.; Zheng,G.Nanoparticle Superlattices as Efficient Bifunctional Electrocatalysts for Water Splitting *J. Am. Chem. Soc.* **2015**, 137, 14305– 14312, DOI: 10.1021/jacs.5b07756

12. Indra, A.; Menezes, P. W.; Driess, M.Uncovering Structure-Activity Relationships in Manganese-Oxide-Based Heterogeneous Catalysts for Efficient Water Oxidation *ChemSusChem* **2015**, 8, 776– 785, DOI: 10.1002/cssc.201402812

13. Chen, D.; Chen, C.; Baiyee, Z. M.; Shao, Z.; Ciucci, F.Nonstoichiometric Oxides as Low-Cost and Highly-Efficient Oxygen Reduction/Evolution Catalysts for Low-Temperature Electrochemical Devices *Chem. Rev.***2015**, 115, 9869– 9921, DOI: 10.1021/acs.chemrev.5b00073

14. Li, C.; Han, X.; Cheng, F.; Hu, Y.; Chen, C.; Chen, J.Phase and Composition Controllable Synthesis of Cobalt Manganese Spinel Nanoparticles towards Efficient Oxygen Electrocatalysis *Nat. Commun.* **2015**, 6,7345, DOI: 10.1038/ncomms8345

15. Cheng, F.; Shen, J.; Ji, W.; Tao, Z.; Chen, J.Selective Synthesis of Manganese Oxide Nanostructures for Electrocatalytic Oxygen Reduction *ACS Appl. Mater. Interfaces* **2009**, 1, 460– 466, DOI: 10.1021/am800131v

16. Meng, Y.; Song, W.; Huang, H.; Ren, Z.; Chen, S.-Y.; Suib, S. L.Structure-Property Relationship of Bifunctional MnO_2 Nanostructures: Highly Efficient, Ultra-Stable Electrochemical Water Oxidation and Oxygen Reduction Reaction Catalysts Identified in Alkaline Media *J. Am. Chem. Soc.* **2014**, 136, 11452– 11464, DOI: 10.1021/ja505186m

17.Duan, J.; Chen, S.; Dai, S.; Qiao, S. Z.Shape Control of Mn_3O_4 Nanoparticles on Nitrogen-Doped Graphene for Enhanced Oxygen Reduction Activity *Adv. Funct. Mater.* **2014**, 24, 2072– 2078, DOI: 10.1002/adfm.201302940

18. Wu, G.; Zelenay, P.Nanostructured Nonprecious Metal Catalysts for Oxygen Reduction Reaction *Acc. Chem. Res.* **2013**, 46, 1878– 1889, DOI: 10.1021/ar400011z

19.Kuo, C.H.; Mosa, I.M.; Thanneeru, S.; Sharma, V.; Zhang, L.; Biswas, S.; Aind ow, M.; Pamir Alpay, S.;Rusling, J. F.; Suib, S. L.Facet-Dependent Catalytic Activity of MnO Electrocatalysts for Oxygen Reduction and Oxygen Evolution Reactions *Chem. Commun.* **2015**, 51, 5951– 5954, DOI: 10.1039/C5CC01152C

20. Zhang, K.; Han, X.; Hu, Z.; Zhang, X.; Tao, Z.; Chen, J.Nanostructured Mn-Based Oxides for Electrochemical Energy Storage and Conversion *Chem. Soc. Rev.* **2015**, 44, 699– 728, DOI: 10.1039/C4CS00218K

21. Huynh, M.; Shi, C.; Billinge, S. J. L.; Nocera, D. G.Nature of Activated Manganese Oxide for Oxygen Evolution *J. Am. Chem. Soc.* **2015**, 137, 14887– 14904, DOI: 10.1021/jacs.5b06382

22. Wang, D.; Chen, X.; Evans, D. G.; Yang, W.Well-Dispersed Co_3O_4/Co_2MnO_4 Nanocomposites as a Synergistic Bifunctional Catalyst for Oxygen Reduction and Oxygen Evolution Reactions *Nanoscale* **2013**,5, 5312– 5315, DOI: 10.1039/c3nr00444a

23. Deng, X.; Tüysüz, H.Cobalt-Oxide-Based Materials as Water Oxidation Catalyst: Recent Progress and Challenges *ACS Catal.* **2014**, 4, 3701– 3714, DOI: 10.1021/cs500713d

24. Deng, X.; Schmidt, W. N.; Tüysüz, H.Impacts of Geometry, Symmetry, and Morphology of Nanocast Co_3O_4 on Its Catalytic Activity for Water Oxidation *Chem. Mater.* **2014**, 26, 6127– 6134, DOI: 10.1021/cm5023163

25. Jin, H.; Wang, J.; Su, D.; Wei, Z.; Pang, Z.; Wang, Y.In Situ Cobalt-Cobalt oxide/N-Doped Carbon Hybrids as Superior Bifunctional Electrocatalysts for Hydrogen and Oxygen Evolution *J. Am. Chem. Soc.* **2015**,137, 2688– 2694, DOI: 10.1021/ja5127165

26. Menezes, P. W.; Indra, A.; González-Flores, D.; Sahraie, N. R.; Zaharieva, I.; Schwarze, M.; Strasser, P.;Dau, H.; Driess, M.High-Performance Oxygen Redox Catalysis with Multifunctional Cobalt Oxide Nanochains: Morphology-Dependent Activity *ACS Catal.* **2015**, 5, 2017– 2027, DOI: 10.1021/cs501724v

27. Lu, X.; Chan, H. M.; Sun, C.-L.; Tseng, C.-M.; Zhao, C.Interconnected Core–shell Carbon Nanotube–graphene Nanoribbon Scaffolds for Anchoring Cobalt Oxides as Bifunctional Electrocatalysts for Oxygen Evolution and Reduction *J. Mater. Chem. A* **2015**, 3, 13371– 13376, DOI: 10.1039/C5TA02967H

28. Maiyalagan, T.; Jarvis, K. A.; Therese, S.; Ferreira, P. J.; Manthiram, A.Spinel-Type Lithium Cobalt Oxide as a Bifunctional Electrocatalyst for the Oxygen Evolution and Oxygen Reduction Reactions *Nat. Commun.* **2014**, 5, 3949, DOI: 10.1038/ncomms4949

29. Su, Y.; Zhu, Y.; Jiang, H.; Shen, J.; Yang, X.; Zou, W.; Chen, J.; Li, C.Cobalt Nanoparticles Embedded in N-Doped Carbon as an Efficient Bifunctional Electrocatalyst for Oxygen Reduction and Evolution Reactions *Nanoscale* **2014**, 6, 15080– 15089, DOI: 10.1039/C4NR04357J

30.Li, B.; Ge, X.; Goh, F.W.T.; Hor, T.S.A.; Geng, D.; Du, G.; Liu, Z.; Zhang, J.; Li u, X.; Zong, Y.Co_3O_4Nanoparticles Decorated Carbon Nanofiber Mat as Binder-Free Air-Cathode for High Performance Rechargeable Zinc-Air Batteries *Nanoscale* **2015**, 7, 1830– 1838, DOI: 10.1039/C4NR05988C

31. Li, C.-S.; Melaet, G.; Ralston, W. T.; An, K.; Brooks, C.; Ye, Y.; Liu, Y.-S.; Zhu, J.; Guo, J.; Alayoglu,S.High-Performance Hybrid Oxide Catalyst of

Manganese and Cobalt for Low-Pressure Methanol Synthesis *Nat. Commun.* **2015**, 6, 6538, DOI: 10.1038/ncomms7538

32. Dang, F.; Oaki, Y.; Kokubu, T.; Hosono, E.; Zhou, H.; Imai, H.Formation of Nanostructured MnO/Co/solid-Electrolyte Interphase Ternary Composites as a Durable Anode Material for Lithium-Ion Batteries *Chem. - Asian J.* **2013**, 8, 760– 764, DOI: 10.1002/asia.201201109

33. Liotta, L. F.; Wu, H.; Pantaleo, G.; Venezia, A. M.Co_3O_4 Nanocrystals and Co_3O_4–MO_x Binary Oxides for CO, CH4 and VOC Oxidation at Low Temperatures: A Review *Catal. Sci. Technol.* **2013**, 3, 3085, DOI: 10.1039/c3cy00193h

34. Liang, H.; Sun, H.; Patel, A.; Shukla, P.; Zhu, Z. H.; Wang, S.Excellent Performance of Mesoporous Co_3O_4/MnO_2 Nanoparticles in Heterogeneous Activation of Peroxymonosulfate for Phenol Degradation in Aqueous Solutions *Appl. Catal., B* **2012**, 127, 330– 335, DOI: 10.1016/j.apcatb.2012.09.001

35. Liang, Y.; Wang, H.; Zhou, J.; Li, Y.; Wang, J.; Regier, T.; Dai, H.Covalent Hybrid of Spinel Manganese-Cobalt Oxide and Graphene as Advanced Oxygen Reduction Electrocatalysts *J. Am. Chem. Soc.* **2012**,134, 3517– 3523, DOI: 10.1021/ja210924t

36. Wang, Y.; Ma, X.; Lu, L.; He, Y.; Qi, X.; Deng, Y.Carbon Supported MnO_x–Co_3O_4 as Cathode Catalyst for Oxygen Reduction Reaction in Alkaline Media *Int. J. Hydrogen Energy* **2013**, 38, 13611– 13616, DOI: 10.1016/j.ijhydene.2013.08.048

37.
Xiao, J.; Wan, L.; Wang, X.; Kuang, Q.; Dong, S.; Xiao, F.; Wang, S.Mesoporous Mn_3O_4–CoO Core–shell Spheres Wrapped by Carbon Nanotubes: A High Performance Catalyst for the Oxygen Reduction Reaction and CO Oxidation *J. Mater. Chem. A* **2014**, 2, 3794– 3800, DOI: 10.1039/c3ta14453d

38. Xu, Y.; Jiang, H.; Li, X.; Xiao, H.; Xiao, W.; Wu, T.Synthesis and Characterization of Mn-Based Composite Oxides with Enhanced Electrocatalytic Activity for Oxygen Reduction *J. Mater. Chem. A* **2014**, 2, 13345–13351, DOI: 10.1039/C4TA02544J

39.Menezes, P.W.; Indra, A.; Sahraie, N.R.; Bergmann, A.; Strasser, P.; Driess, M.Cobalt-Manganese-Based Spinels as Multifunctional Materials That Unify

Catalytic Water Oxidation and Oxygen Reduction Reactions*ChemSusChem* **2015**, 8, 164– 171, DOI: 10.1002/cssc.201402699

40. Li, G.; Zhang, K.; Mezaal, M. A.; Lei, L.Synthesis and Electrocatalytic Performance of Co_3O_4 Modified Mn_3O_4 Composites for Zinc-Air Batteries Synthesis and Electrocatalytic Performance of NiO Modified Co_3O_4 Composites for Zinc-Air Batteries *Int. J. Electrochem. Sci.* **2015**, 10, 10554– 10564

41. Huang, W.; Zhong, H.; Li, D.; Tang, P.; Feng, Y.Reduced Graphene Oxide Supported CoO/MnO_2Electrocatalysts from Layered Double Hydroxides for Oxygen Reduction Reaction *Electrochim. Acta* **2015**,173, 575– 580, DOI: 10.1016/j.electacta.2015.05.095

42. Du, J.; Chen, C.; Cheng, F.; Chen, J.Rapid Synthesis and Efficient Electrocatalytic Oxygen Reduction/Evolution Reaction of $CoMn_2O_4$ Nanodots Supported on Graphene *Inorg. Chem.* **2015**, 54,5467– 5474, DOI: 10.1021/acs.inorgchem.5b00518

43. Ge, X.; Liu, Y.; Goh, F. W. T.; Hor, T. S. A.; Zong, Y.; Xiao, P.; Zhang, Z.; Lim, S. H.; Li, B.; Wang, X.Dual-Phase Spinel $MnCo_2O_4$ and Spinel $MnCo_2O_4$/nanocarbon Hybrids for Electrocatalytic Oxygen Reduction and Evolution *ACS Appl. Mater. Interfaces* **2014**, 6, 12684– 12691, DOI: 10.1021/am502675c

44. Yu, T.; Moon, J.; Park, J.; Park, Y. I.; Na, H. B.; Kim, B. H.; Song, I. C.; Moon, W. K.; Hyeon, T.Various-Shaped Uniform Mn_3O_4 Nanocrystals Synthesized at Low Temperature in Air Atmosphere *Chem. Mater.***2009**, 21, 2272– 2279, DOI: 10.1021/cm900431b

45. Li, Y.; Zhou, W.; Wang, H.; Xie, L.; Liang, Y.; Wei, F.; Idrobo, J.-C.; Pennycook, S. J.; Dai, H.An Oxygen Reduction Electrocatalyst Based on Carbon Nanotube–graphene Complexes *Nat. Nanotechnol.* **2012**, 7,394– 400, DOI: 10.1038/nnano.2012.72

46. Hosseini, S. a.; Niaei, a.; Salari, D.; Nabavi, S. R.Nanocrystalline AMn_2O_4 (A = Co, Ni, Cu) Spinels for Remediation of Volatile Organic Compounds—synthesis, Characterization and Catalytic Performance*Ceram. Int.* **2012**, 38, 1655– 1661, DOI: 10.1016/j.ceramint.2011.09.057

47.Hosseini, S.A.; Salari, D.; Niaei, A.; Deganello, F.; Pantaleo, G.; Hojati, P.Che mical-Physical Properties of Spinel $CoMn_2O_4$ Nano-Powders and Catalytic Activity in the 2-Propanol and Toluene Combustion: Effect of the Preparation Method *J.*

Environ. Sci. Health, Part A: Toxic/Hazard. Subst. Environ. Eng. **2011**, 46,291–297, DOI: 10.1080/10934529.2011.539093

48. Sexton, B. A.; Hughes, A. E.; Turney, T. W.An XPS and TPR Study of the Reduction of Promoted Cobalt-Kieselguhr Fischer–Tropsch Catalysts *J. Catal.* **1986**, 97, 390– 406, DOI: 10.1016/0021-9517(86)90011-4

49. Arnoldy, P.Temperature-Programmed Reduction of CoO/Al_2O_3 Catalysts *J. Catal.* **1985**, 93, 38– 54, DOI: 10.1016/0021-9517(85)90149-6

50. Brown, R.; Cooper, M. E.; Whan, D. A.Temperature Programmed Reduction of Alumina-Supported Iron, Cobalt and Nickel Bimetallic Catalysts *Appl. Catal.* **1982**, 3, 177– 186, DOI: 10.1016/0166-9834(82)80090-0

51. Lin, H. Y.; Chen, Y. W.The Mechanism of Reduction of Cobalt by Hydrogen *Mater. Chem. Phys.* **2004**, 85,171– 175, DOI: 10.1016/j.matchemphys.2003.12.028

52. Sytnyk, M.; Kirchschlager, R.; Bodnarchuk, M. I.; Primetzhofer, D.; Kriegner, D.; Enser, H.; Stangl, J.;Bauer, P.; Voith, M.; Hassel , A.Tuning the Magnetic Properties of Metal-Oxide Nanocrystal Heterostructures by Cation Exchange *Nano Lett.* **2013**, 13, 586– 593, DOI: 10.1021/nl304115r

53. Gutmann, V. *Coordination Chemistry in Non-Aqueous Solutions*; Springer Vienna: Vienna, **1968**.

54. Trutia, A.Optical Spectra of Divalent Cobalt Complexes *J. Optoelectron. Adv. Mater.* **2005**, 7, 2677–2686

55. Fine, A.Halide Complexes of Cobalt (II) in Acetone Solution *J. Am. Chem. Soc.* **1962**, 84, 1139– 1144,DOI: 10.1021/ja00866a016

56. Shinagawa, T.; Garcia-Esparza, A. T.; Takanabe, K.Insight on Tafel Slopes from a Microkinetic Analysis of Aqueous Electrocatalysis for Energy Conversion *Sci. Rep.* **2015**, 5, 13801, DOI: 10.1038/srep13801

57. Roche, I.; Chaînet, E.; Chatenet, M.; Vondrák, J.Carbon-Supported Manganese Oxide Nanoparticles as Electrocatalysts for the Oxygen Reduction Reaction (ORR) in Alkaline Medium: Physical Characterizations and ORR Mechanism *J. Phys. Chem. C* **2007**, 111, 1434– 1443, DOI: 10.1021/jp0647986

58. Bard, A. J.; Faulkner, L. R. *Electrochemical Methods: Fundamentals and Applications*, 2nd ed.; Wiley:New York, **2001**.

59. Chatenet, M.; Aurousseau, M.; Durand, R.; Andolfatto, F.Silver-Platinum Bimetallic Catalysts for Oxygen Cathodes in Chlor-Alkali Electrolysis: Comparison with Pure Platinum *J. Electrochem. Soc.* **2003**, 150,D47– D55, DOI: 10.1149/1.1540063

60.Chatenet, M.; GeniesBultel, L.; Aurousseau, M.; Durand, R.; Andolfatto, F.Oxy gen Reduction on Silver Catalysts in Solutions Containing Various Concentrations of Sodium Hydroxide - Comparison with Platinum *J. Appl. Electrochem.* **2002**, 32, 1131– 1140, DOI: 10.1023/A:1021231503922

61. Cherevko, S.; Zeradjanin, A. R.; Keeley, G. P.; Mayrhofer, K. J. J.A Comparative Study on Gold and Platinum Dissolution in Acidic and Alkaline Media *J. Electrochem. Soc.* **2014**, 161, H822– H830, DOI: 10.1149/2.0881412jes

62. Gong, M.; Li, Y.; Wang, H.; Liang, Y.; Wu, J. Z.; Zhou, J.; Wang, J.; Regier, T.; Wei, F.; Dai, H.An Advanced Ni-Fe Layered Double Hydroxide Electrocatalyst for Water Oxidation *J. Am. Chem. Soc.* **2013**, 135, 8452–8455, DOI: 10.1021/ja4027715

63. Smith, R. D. L.; Prévot, M. S.; Fagan, R. D.; Zhang, Z.; Sedach, P. A.; Siu, M. K. J.; Trudel, S.;Berlinguette, C. P.Photochemical Route for Accessing Amorphous Metal Oxide Materials for Water Oxidation Catalysis *Science* **2013**, 340, 60– 63, DOI: 10.1126/science.1233638

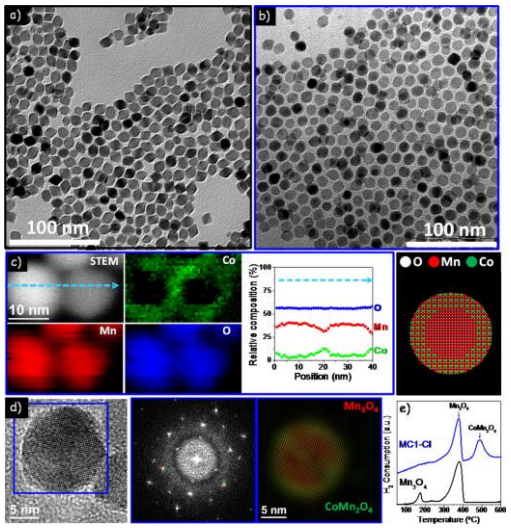

Figure 1. TEM micrographs of Mn_3O_4 NPs (a) and MC1-Cl NPs (b). (c) ADF-STEM image and EELS elemental mapping of MC1-Cl NPs and compositional line profile of Mn, Co, and O elements recorded along the arrow in the STEM images. (d) HRTEM micrograph of a MC1-Cl NP, power spectra of the blue squared region, and colorful structural map showing the distribution of Mn_3O_4 (red) and $CoMn_2O_4$ (green) phases. (e) H_2 TPR profile of $Mn_3O_4$and MC1-Cl NPs.

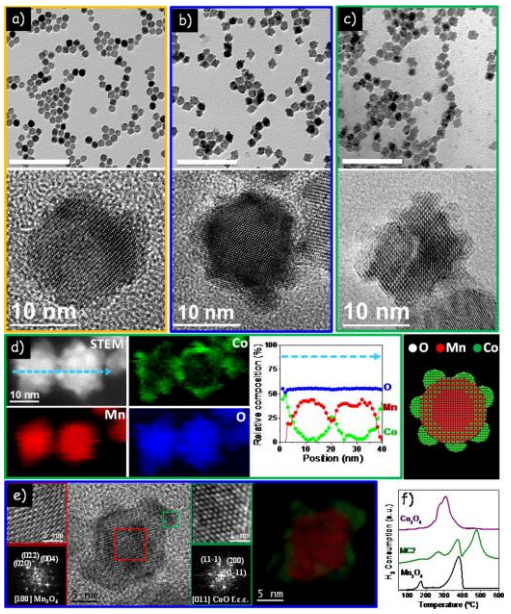

Figure 2. TEM (scale bar = 100 nm) and HRTEM micrographs of MC0.5 (a), MC1 (b), and MC2 (c) NPs. (d) ADF-STEM image and EELS elemental mapping of MC2 NPs and compositional line profile of Mn, Co, and O elements recorded along the arrow in the STEM image. (e) HRTEM micrographs of a MC1 NP, details of the red and green squared regions with the corresponding power spectra, and colorful structural map showing the distribution of body centered tetragonal Mn_3O_4 (red) and face centered cubic CoO (green) phases. (f) H_2 TPR profile of Mn_3O_4, MC2, and Co_3O_4 NPs.

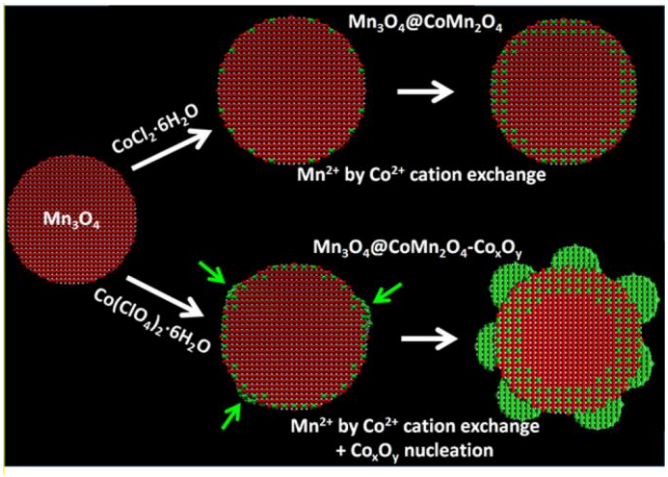

Figure 3. Scheme of the formation of the Mn_3O_4@$CoMn_2O_4$ and Mn_3O_4@$CoMn_2O_4$–Co_xO_y nano-heterostructures when using either a cobalt chloride or a cobalt perchlorate solution. Mn_3O_4@$CoMn_2O_4$ NPs were obtained by partial cation exchange between Mn^{2+} and Co^{2+} when using a cobalt chloride precursor. Mn_3O_4@$CoMn_2O_4$–Co_xO_y NPs were obtained by the same cation exchange reaction and the additional and simultaneous nucleation of a Co_xO_y phase when using a cobalt perchlorate. Green arrows in the bottom cartoon point at Co_xO_y nanocrystal nucleation sites.

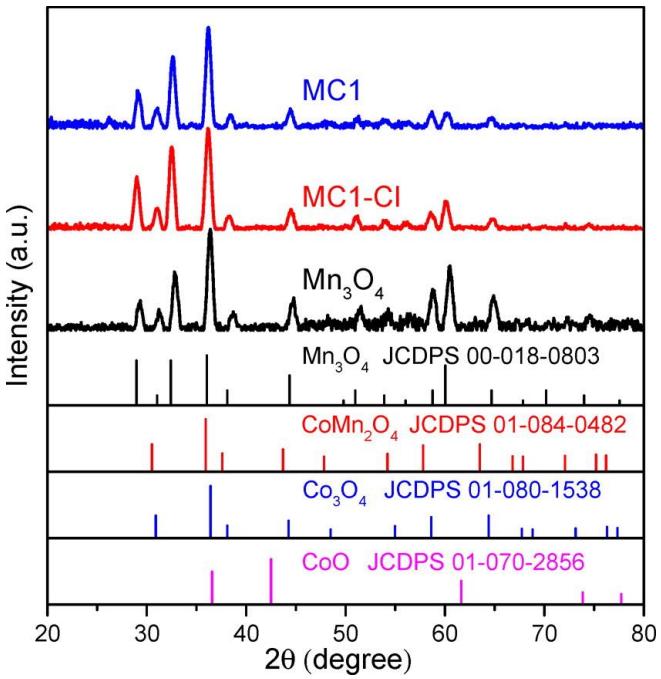

Figure 4. XRD patterns of as-synthesized, Mn_3O_4 and Mn–Co oxide NPs.

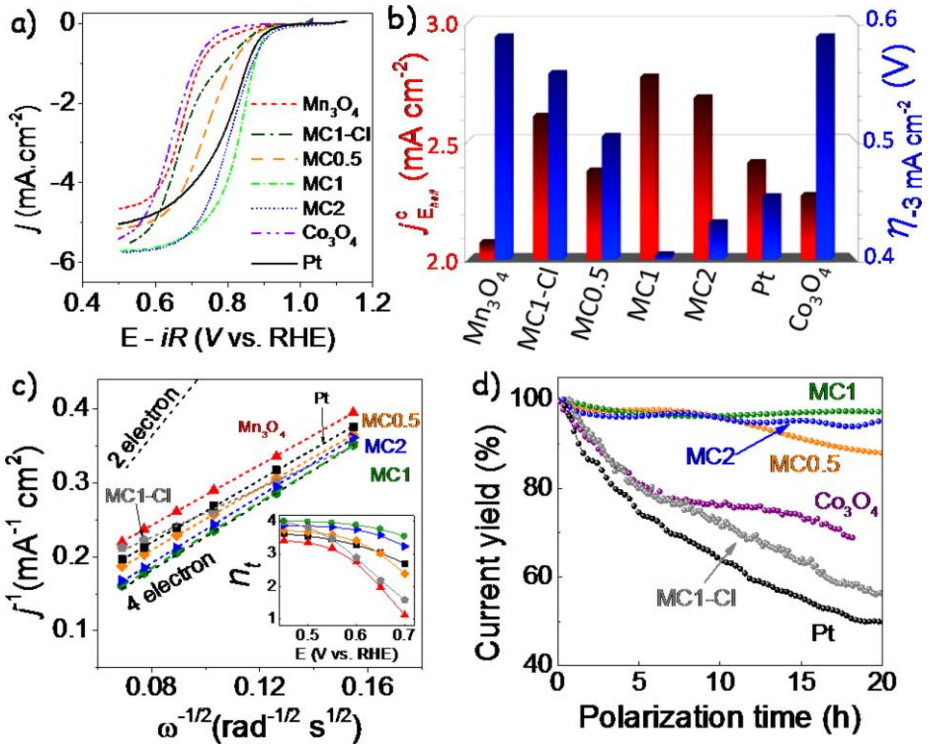

Figure 5. (a) ORR polarization curves of MC/C, Mn_3O_4/C, Co_3O_4/C, and Pt/C in O_2-saturated 0.1 M KOH at 1600 rpm using a scan rate of 5 mV/s. (b) Kinetic current densities at half-wave potential (red) and overpotentials (blue). (c) K–L plots at 0.5 V versus RHE. The standard lines for two- and four-electron pathways are also plotted as a guideline. Inset shows n_t at different potentials. (d) Chronoamperometric data at 0.79 V in O_2-saturated 0.1 M KOH.

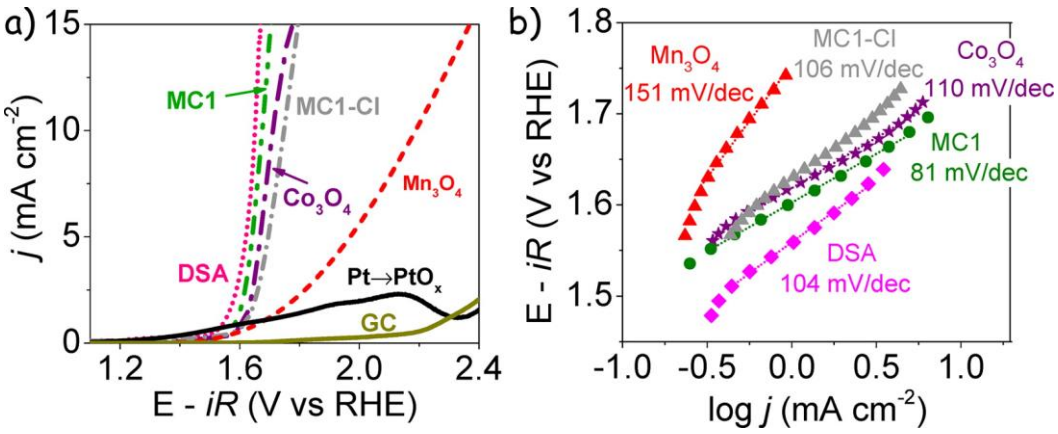

Figure 6. (a) OER polarization curves of Mn_3O_4/C, Co_3O_4/C, MC/C, Pt/C, DSA, and glassy carbon (GC) in O_2-saturated 0.1 M KOH at a scan rate of 5 mV/s. (b) Tafel plots derived from OER polarization curves.